Spatial and Seasonal Variations in Aridification across Southwest North America

SHANNON M. JONES AND DAVID S. GUTZLER

University of New Mexico, Albuquerque, New Mexico

(Manuscript received 15 December 2014, in final form 28 October 2015)

ABSTRACT

Southwestern North America (SWNA) is projected to become drier in the twenty-first century as both precipitation (P) and evaporation (E) rates change with increasing greenhouse gas concentration. The authors diagnose the relative contributions of changes in P and E to the local surface moisture balance ($P - E$) in cold and warm halves of the year across SWNA. Trends in $P - E$ vary spatially between the arid southern subregion (mostly northern Mexico) and the more temperate northern subregion (southwest United States), although both subregions exhibit a negative trend in $P - E$ (trending toward more arid conditions) in CMIP5 projections for the twenty-first century. The $P - E$ trend is biggest in the cold season, when much of the base flow to rivers in the southwest United States is generated. The downward trend in cold season $P - E$ across SWNA is caused primarily by increasing E in the north and decreasing P in the south. Decreasing P is the primary contributor to modest warm season drying trends in both northern and southern subregions. Also, P accounts for most of the interannual variability in SWNA $P - E$ and is strongly correlated with modes of oceanic natural variability during the cold season. SWNA aridification is therefore most readily distinguished from the region's large natural climate variability in the cold season in the northern subregion, where the projected temperature-driven increase in E is greater than the projected decrease in P.

1. Introduction

Climate model projections indicate that arid conditions throughout southwestern North America (SWNA) will amplify over the next century as a function of long-term trends in precipitation (P) and evaporation (E) (Seager et al. 2007; Hoerling and Eischeid 2007; Gutzler and Robbins 2011; Cook et al. 2015). Increasing evidence suggests this is already happening (Garfin et al. 2014), although detecting long-term trends distinct from episodic droughts in real time is difficult (e.g., Cayan et al. 2010; Seager and Vecchi 2010; Seneviratne et al. 2012). Anthropogenic global warming has induced observed and simulated changes in western hydrology, including parts of SWNA, since the latter half of the twentieth century (Barnett et al. 2008; Cayan et al. 2010). Some of the hottest and driest years on record for SWNA occurred during the early twenty-first century, even though precipitation anomalies have remained within the range of natural variability (Barnett et al. 2008).

Distinguishing the signal of a long-term trend in aridity from a transient multiyear drought is an important climate monitoring challenge, as exemplified by debate over the causes of extreme drought in California (Wang et al. 2014; Seager et al. 2015). Drought, defined as a precipitation deficit below the climatological average, is a normal part of the natural climate variability of SWNA (Woodhouse et al. 2010). Precipitation across SWNA fluctuates on interannual to multidecadal time scales and is modulated by remote sea surface temperature anomalies in the Pacific and Atlantic Oceans (Ropelewski and Halpert 1986; McCabe et al. 2004; Schubert et al. 2009; Seager et al. 2005). Regional droughts of the 1930s, 1950s, and early 2000s are examples of persistent drought conditions that have severely affected regional hydrology, ecosystems, and economies across SWNA (Swetnam and Betancourt 1998; Weiss et al. 2009).

However, unlike the episodic ocean-forced precipitation deficits that characterize historical SWNA drought, projected twenty-first century aridification represents a transition to sustained drier conditions that will inhibit drought recovery in the future (Gutzler and Robbins 2011; Cook et al. 2015). SWNA aridification is consistent with observed and simulated global trends,

Corresponding author address: D. S. Gutzler, Department of Earth and Planetary Sciences, University of New Mexico MSC03-2040, Albuquerque, NM 87131-0001.
E-mail: gutzler@unm.edu

DOI: 10.1175/JCLI-D-14-00852.1

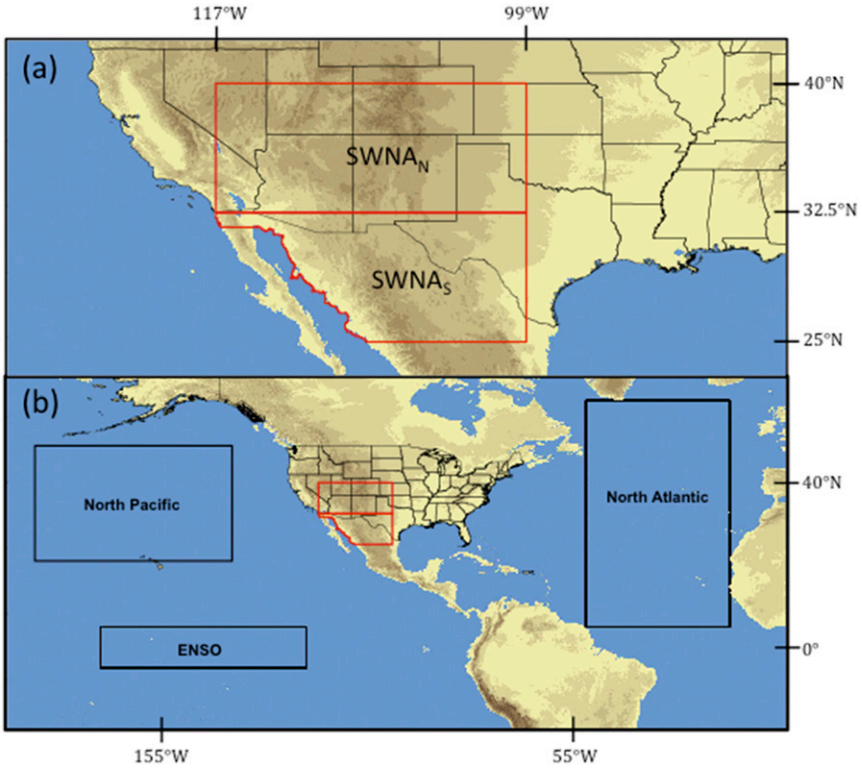

FIG. 1. (a) The spatial extent of subregions SWNA North (32.5°–40°N, 117°–99°W), SWNA South (25°–32.5°N, 117°–99°W), and the entire (North + South) SWNA. Precipitation (P) and latent heat flux (converted to evaporation, E) values are averaged across all model grid cells that are located completely within or <1° outside of the boundaries of the averaging areas. Grid cells containing less than 80% land surface area are not included in the spatial averages. (b) Averaging regions for temperature in the North Atlantic (5°–60°N, 52°–17°W), North Pacific (21°–49°N, 186°–138°W), and tropical Pacific (5°S–5°N, 170°–120°W), configured to capture simulated climate variability associated with the Atlantic multidecadal oscillation, the Pacific decadal oscillation, and El Niño–Southern Oscillation, respectively.

sometimes described as wet regions getting wetter and dry regions getting drier (Held and Soden 2006; IPCC 2013). In subtropical North America the dynamics of aridification have been described in terms of the poleward extension of the Hadley circulation and expansion of the subtropical dry zone as the climate warms (Yin 2005; Seidel et al. 2008), or alternatively as the regional response to shifts in planetary waves (Seager et al. 2014).

Hydroclimate varies both spatially and seasonally across SWNA. The contribution of cold season P to the annual total is large for the northern (southwest United States) half of SWNA, where the headwaters of major southwestern U.S. rivers originate and are fed by snowmelt runoff (Fig. 1). The warm season P contribution is higher in the southern half of SWNA (mostly northern Mexico), where the North American monsoon is centered (Douglas et al. 1993). Projections from phase 3 of the Coupled Model Intercomparison Project (CMIP3) indicate that an annually averaged downward trend in the twenty-first-century surface moisture balance ($P - E$) is caused by an average decrease in P over a large area of SWNA, including both the northern and southern subregions alluded to above (Seager et al. 2007). However, Gutzler and Robbins (2011) describe a drying trend in CMIP3 projections across the southwestern United States that is associated with a temperature-driven increase in E, while the projected trend in P is statistically indistinguishable from zero.

The purpose of the present analysis is to reassess the spatial and seasonal aspects of projected SWNA aridification to clarify this apparent discrepancy, and to diagnose the relative roles of P and E in projected aridification as a function of latitude and season. As suggested by previous studies, the major long-term climate change trend in observations is in temperature, which strongly modulates the E term in the surface water budget, whereas P is the term that exhibits the

TABLE 1. CMIP5 models used in this analysis and their horizontal resolutions. A single iteration from the historical and RCP8.5 simulations is analyzed for each of the 18 models in the ensemble. (Expansions of acronyms are available online at http://www.ametsoc.org/PubsAcronymList.)

Model	Modeling center	Model resolution
ACCESS1.0	Commonwealth Scientific and Industrial Research Organization; Bureau of Meteorology	1.25° × 1.875°
ACCESS1.3	Commonwealth Scientific and Industrial Research Organization; Bureau of Meteorology	1.25° × 1.875°
BNU-ESM	College of Global Change and Earth System Science, Beijing Normal University	2.81° × 2.81°
CCSM4	National Center for Atmospheric Research	0.94° × 1.25°
CESM1-BGC	National Center for Atmospheric Research	0.94° × 1.25°
CESM1-CAM5	National Center for Atmospheric Research	0.94° × 1.25°
CSIRO-Mk3.6	Commonwealth Scientific and Industrial Research Organization in collaboration with Queensland Climate Change Center of Excellence	1.875° × 1.875°
FGOALS-G2.0	Institute of Atmospheric Physics, Chinese Academy of Sciences, Tsinghua University	3° × 2.81°
GFDL-CM3	NOAA Geophysical Fluid Dynamics Laboratory	2° × 2.5°
GISS-E2-H	NASA Goddard Institute for Space Studies	2° × 2.5°
GISS-E2-R	NASA Goddard Institute for Space Studies	2° × 2.5°
HadGEM2-ES	Met Office Hadley Center	1.25° × 1.875°
INM-CM4	Institute for Numerical Mathematics	1.5° × 2°
IPSL-CM5A-MR	Institut Pierre-Simon Laplace	1.26° × 2.5°
MIROC5	Atmosphere and Ocean Research Institute, National Institute for Environmental Studies; Japan Agency for Marine-Earth Science and Technology	1.4° × 1.4°
MPI-ESM-LR	Max Planck Institute for Meteorology	1.875° × 1.875°
MRI-CGCM3	Meteorological Research Institute	1.125° × 1.125°
NorESM1-M	Norwegian Climate Centre	1.875° × 2.5°

largest natural variability on interannual and decadal time scales, identified as drought and pluvial episodes. By parsing the trends in P, E, and $P - E$ by season and subregion, we show significant spatial and seasonal differences in the processes contributing to SWNA aridification. Trends are analyzed in the context of interannual and decadal variability, emphasizing distinctions between the signals associated with episodic drought and long-term aridification.

2. Models and methods

Trends and variability in precipitation (P), evaporation (E), and the net vertical flux of water into the surface ($P - E$) are analyzed using an ensemble of 18 climate models (Table 1) from phase 5 of the Coupled Model Intercomparison Project (CMIP5) archive (Taylor et al. 2012). All simulations considered are generated from the CMIP5 historical and representative concentration pathway 8.5 (RCP8.5) experiments (Moss et al. 2010), using a single iteration per model. Simulations from the historical period (1861–2005) are forced with estimated solar irradiance, natural and anthropogenic aerosols, and historical greenhouse gas concentration. Projected twenty-first-century simulations (2006–2100) are all forced by a scenario of prescribed future solar irradiance and aerosols, and greenhouse gas concentration derived from an emissions pathway that increases anthropogenic radiative forcing by 8.5 $W m^{-2}$ relative to preindustrial conditions by the year 2100 (RCP8.5; Moss et al. 2010; Meinshausen et al. 2011; IPCC 2013).

Model output includes P (CMIP5 variable pr) and latent heat flux (CMIP5 variable hfls) values in monthly increments. The latent heat flux is converted to a water flux (evaporation, E) using a constant value for the latent heat of vaporization (2.5×10^6 J kg^{-1}). Values of P and E are converted to units of mm $month^{-1}$. We calculate the net vertical flux of water into the ground surface as the difference P minus E. This difference approximates a surface moisture balance, to the extent that the horizontal and subsurface vertical moisture fluxes are negligible when calculating monthly $P - E$ at the top of a column extending downward from the ground surface. The surface moisture balance can also be approximated as the difference between moisture convergence and divergence within a column of air extending upward from the ground surface (Seager et al. 2007). Calculating $P - E$ directly from the surface moisture fluxes P and E allows us to differentiate the cause of trends in $P - E$ and to interpret important seasonal differences between warm and cold season aridification across the climatically variable landscape of SWNA.

The CMIP5 global models are designed to capture large-scale features of climate change. More detailed analyses of simulations of SWNA climate using global models (e.g., Seager et al. 2007; Gutzler et al. 2009; Cook

and Seager 2013; and many others) have shown that there is considerable subregional variability among models with respect to features such as temperature and precipitation gradients and timing of monsoon onset. Accordingly we have chosen to average the CMIP5 output in space and time to focus on relatively large scales, while retaining the large-scale differences between cold (December–May) and warm season (June–November) precipitation, and the important snow-affected area to the north versus the warmer and more strongly monsoonal climate to the south.

We define the SWNA region as the land surface area bounded by 25°–40°N, 99°–117°W, which includes most of the southwestern United States and northern Mexico (Fig. 1a). This area shares the same northern and southern boundaries as the region considered by Seager et al. (2007). We divide SWNA into northern and southern subregions at latitude 32.5°N, near the U.S.–Mexico border (Fig. 1a). The northern subregion (hereafter SWNA North or just North) encompasses the more temperate areas of the southwestern United States. Cold season P, much of which falls as snow in higher elevations, accounts for >50% of the annual precipitation total in the northern and western parts of this subregion (NOAA 2014). The southern subregion (hereafter SWNA South or just South) encompasses the more arid parts of SWNA, including northern Mexico. Within this subregion warm season precipitation, much of which falls during the monsoon season, accounts for up to 60%–80% of the annual total in the southern and eastern parts of the subregion (NOAA 2014; Douglas et al. 1993). We use these regions to characterize the large-scale spatial variability of aridification across southwestern North America. Our goal is to distinguish the important large-scale north–south climatic differences within SWNA, while retaining sufficient area to average over multiple model grid cells in each subregion.

For each model, the monthly values of P and E are averaged spatially across the North and South subregions (and their sum, the entire SWNA) by calculating the mass-weighted mean of whole grid cells located completely within or <1° outside the boundaries of the averaging regions. Output from grid cells containing ≥20% ocean surface are not included in the spatial averages. For a model with 1.25° × 1.875° resolution (as an example), 93 grid cells contribute to the average for the entire SWNA.

Time series of the spatially averaged seasonal P and E are produced for North, South and the entire SWNA by calculating the mean of the monthly P and E spatial averages over every cold (December–May) and warm (June–November) half-yearly ''seasons'' from 1861–2100. The cold half-year includes the snow accumulation and ablation season in the North (Serreze et al. 1999). The warm half-year includes the monsoon season across SWNA, the onset date and duration of which vary from South to North (Higgins et al. 1999). During some years, considerable precipitation from tropical cyclone remnants occurs during this half year (Larson et al. 2005). The resulting time series are annual values of P or E averaged across North, South, or SWNA for the cold season (North/Cold, South/Cold and SWNA/Cold) or the warm season (North/Warm, South/Warm, SWNA/Warm), for each model.

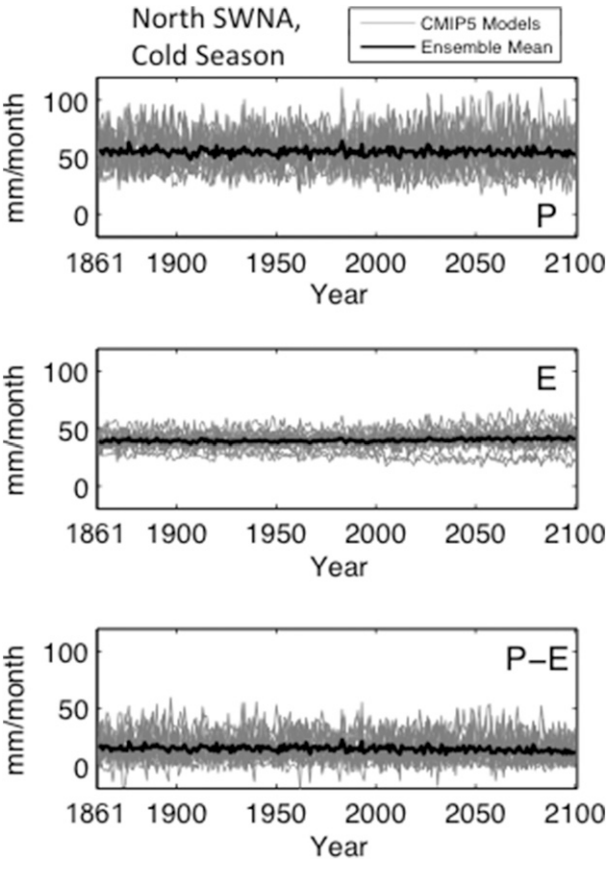

FIG. 2. Time series of cold season (top) P, (middle) E, and (bottom) $P - E$ for SWNA North (mm month^{-1}) for each of the 18 CMIP5 models (gray lines) plus the ensemble mean (black lines). Historical (1861–2005) and RCP8.5 (2006–2100) simulations are concatenated to form continuous time series from 1861–2100.

Time series of spatially averaged half-yearly P and E from the historical and future RCP8.5 periods are concatenated to form continuous time series (1861–2100) for each model, as shown in Fig. 2 for North/Cold. Climatologies of P and E are calculated for the initial century of the historical period (1861–1960) to estimate the simulated average before atmospheric CO_2

TABLE 2. Regression coefficients for the 1861–2100 linear trends in the 18-model ensemble mean precipitation ($\overline{P}$), evaporation ($\overline{E}$), and surface moisture balance ($\overline{P-E}$). Model biases were removed by subtracting the 1861–1960 mean from each time series before calculating $\overline{P}$, $\overline{E}$, and $\overline{P-E}$. Linear trends are calculated for the SWNA North and South, and the entire (North + South) region (denoted SWNA), separately for cold (December–May) and warm (June–November) half yearly seasons. The annually averaged linear trend across the entire SWNA (SWNA/Annual) is shown. All trends are statistically significant ($\alpha = 0.05$) except for North/Cold $\overline{P}$ (in parentheses).

1861–2100 linear trends (mm month^{-1} century^{-1})			
	$\overline{P}$	$\overline{E}$	$\overline{P-E}$
North/Cold	(−0.3)	0.9	−1.2
South/Cold	−4.9	−2.7	−2.2
SWNA/Cold	−2.3	−0.7	−1.6
North/Warm	−1.8	−1.3	−0.5
South/Warm	−2.7	−2.1	−0.5
SWNA/Warm	−2.2	−1.7	−0.5
SWNA/Annual	−2.3	−1.2	−1.1

concentration and global temperatures began to increase rapidly in the late twentieth century. The 1861–1960 mean P or E value is subtracted from each corresponding 1861–2100 time series, thereby removing systematic model biases to facilitate comparison of variance and trends between simulations. Hereafter we refer to the 1861–2100 spatially averaged seasonal P and E time series with model biases removed as the ''normalized'' time series.

The normalized P and E time series are used to calculate $P - E$ for each model as well as annual values of the 18-model ensemble mean $\overline{P}$ or $\overline{E}$, mean surface moisture balance $\overline{P-E}$, and the entire 18-model ensemble $(P-E)'$ interquartile range (25th to 75th percentiles), for the two half-yearly seasons and each averaging region. Secular trends in $\overline{P}$, $\overline{E}$, and $\overline{P-E}$ are quantified via linear regression (Table 2), where the year is the independent variable. Gutzler and Robbins (2011) showed that linear change with time is a good assumption in projections of temperature and precipitation using CMIP3 simulations driven by the A1B emissions scenario; our analysis indicates that this simplification also captures century-scale variability in CMIP5 simulations. Temporal trend significance is assessed against a null hypothesis of zero using a two-tailed t test at the 5% significance level.

To explore the mechanisms that generate SWNA interannual variability within the CMIP5 simulations, we analyze the correlations between SWNA P and ocean surface air temperature anomalies (T; CMIP5 variable tas) in regions associated with the Atlantic multidecadal oscillation (AMO), the Pacific decadal oscillation (PDO), and El Niño–Southern Oscillation (ENSO).

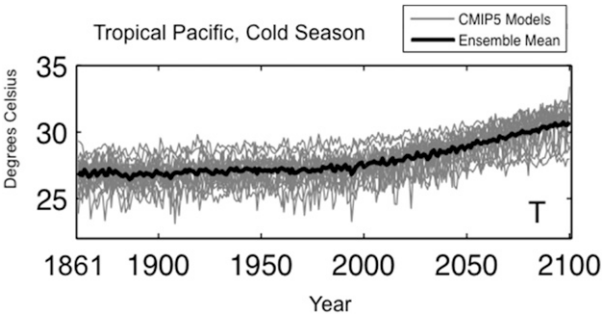

FIG. 3. Time series of cold season tropical Pacific (TPac) Ocean surface air temperature (°C) for each of the 18 CMIP5 models (gray lines) plus the ensemble mean (black line). Historical (1861–2005) and RCP8.5 (2006–2100) simulations are concatenated to form continuous time series from 1861–2100.

Whether ENSO and PDO represent distinct modes of oceanic variability is a topic of current research that is beyond the scope of this study; here we simply use geographically distinct temperature averaging areas over the North Pacific and tropical Pacific to examine whether CMIP5 models reproduce observed correlations with SWNA precipitation.

We use tas to represent oceanic temperature, having checked that interannual variability of monthly tas values is uniformly highly correlated with collocated ocean temperature tos, as expected. Monthly values of T are averaged spatially across the North Atlantic (NA: 5°–60°N, 52°–17°W), North Pacific (NP: 21°–49°N, 186°–138°W), and tropical Pacific (TP: 5°S–5°N, 170°–120°W) oceans to represent AMO, PDO, and ENSO climate variability indices, respectively (Fig. 1b). Previous analyses have shown that CMIP5 models in aggregate simulate the general features of large-scale variability in the Pacific and Atlantic basins associated with these phenomena (Stevenson 2012; Kim et al. 2012; Bellenger et al. 2014).

Detrended P time series are calculated for North/Cold, South/Cold, North/Warm, and South/Warm by removing the linear trend from the unprocessed (not normalized) historical and RCP8.5 P time series for each model. The individual model monthly NA, NP, and TP T time series are averaged over each cold (NA/Cold, NP/Cold, and TP/Cold) and warm (NA/Warm, NP/Warm, and TP/Warm) season within the historical and RCP8.5 periods for each model. Cold season TP time series of T (1861–2100) for each model plus the ensemble mean show the spread of the 18-model output (Fig. 3). Cold season TP T values increase rapidly beginning in the year 2006 when the anthropogenic radiative forcing starts to follow the RCP8.5 pathway. Trends in T are subtracted from the time series to separate the variance associated with the linear trend from

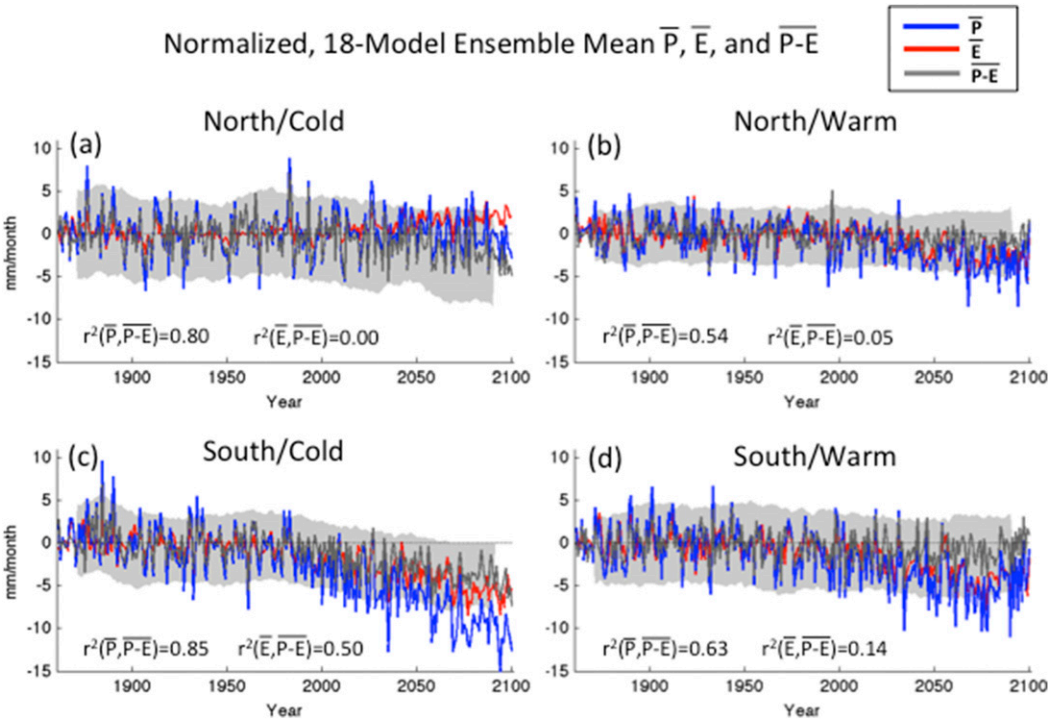

FIG. 4. The 18-model ensemble mean anomalies of $\overline{P}$ (blue), $\overline{E}$, (red), and $\overline{P-E}$ (dark gray) (mm month^{-1}) are shown for SWNA North and South during the cold (December–May) and warm (June–November) half-year seasons; $\overline{P}$, $\overline{E}$, and $\overline{P-E}$ are shown relative to their 1861–1960 simulated historical means ($y = 0$). The 25th to 75th percentile range of $P - E$ over the entire 18-model ensemble is shown as a smoothed envelope using a 21-yr centered moving average (light gray shading). Historical (1861–2005) and RCP8.5 (2006–2100) simulations are concatenated to form continuous time series from 1861–2100. The fraction of total variance in $\overline{P-E}$ that is accounted for by $\overline{P}$ and by $\overline{E}$ is shown for each subregion and season.

the total variance, similar to the processing carried out for continental P and E time series. Hereafter we refer to the spatially averaged seasonal ocean surface air temperatures with trends removed as the detrended T time series.

Correlations between the detrended T and detrended P time series for each subregion and season are calculated for each of the 18 models. Correlations between TP T and NP T describe the extent to which CMIP5 models capture observed covariability of ENSO and PDO indices and their influence on climate variability in SWNA. Correlation coefficients r are considered significant if the null hypothesis of zero correlation is rejected at $\alpha = 0.05$ and if r agrees in sign with observation-based results: $r > 0$ for r(SWNA P, TP T), and $r < 0$ for r(SWNA P, NP T), r(SWNA P, NA T), and r(TP T, NP T) (McCabe et al. 2004; Ropelewski and Halpert 1986; Gershunov and Barnett 1998).

3. Historical and projected trends in P, E, and $P - E$

An overall decrease in $\overline{P-E}$ (trending toward aridity) occurs across both North and South subregions, in both the warm and cold half-year seasons (Fig. 4). The biggest decrease in $\overline{P-E}$ occurs during the twenty-first century (RCP8.5) portion of each time series. The downward trend in $\overline{P-E}$ is especially pronounced in South/Cold, where the trend in $\overline{P}$ (-4.9 mm month^{-1} century^{-1}) decreases faster than the compensating trend in $\overline{E}$ (-2.7 mm month^{-1} century^{-1}) (Fig. 4c, Table 2). In North/Cold, increasing $\overline{E}$ (0.9 mm month^{-1} century^{-1}) causes the downward trend in $\overline{P-E}$ (-1.2 mm month^{-1} century^{-1}), while there is a small but statistically insignificant trend in $\overline{P}$ (-0.3 mm month^{-1} century^{-1}) (Fig. 4a, Table 2). It is worth noting that the full spread of linear trends among the 18-model ensemble includes both positive and negative regression coefficient values, as shown for North/Cold in Table 3. This range includes individual model trends that differ in sign from the ensemble mean trends (Table 3).

There are smaller but notable downward warm season trends in $\overline{P-E}$ (-0.5 mm month^{-1} century^{-1}) for both North/Warm and South/Warm, where the trend in $\overline{P}$ (-1.8 and -2.7 mm month^{-1} century^{-1}, respectively) decreases faster than the trend in $\overline{E}$ (-1.3 and -2.1 mm month^{-1} century^{-1}, respectively) (Figs. 4b,d, Table 2). Note that $\overline{P}$

TABLE 3. Regression coefficients for the 1861–2100 linear trends in cold season (December–May) precipitation (P), evaporation (E), and the surface moisture balance ($P - E$) for SWNA North, for each simulation considered, with the means of all trend coefficients shown at the bottom. Time series have been normalized for each model by subtracting their respective 1861–1960 mean value in order to remove model biases. The minimum and maximum trend values among the 18 CMIP5 models are shown in bold for P, E, and $P - E$ to highlight the full spread of trends.

North/Cold 1861–2100 trend comparison (mm month^{-1} century^{-1})			
Model	P	E	$P - E$
ACCESS 1.0	−2.5	−1.7	−0.8
ACCESS 1.3	1.1	0.9	0.3
BNU-ESM	−2.9	2.7	**−5.6**
CCSM4	4.0	3.2	0.8
CESM1-BGC	2.1	2.8	−0.7
CESM1-CAM5	1.6	2.5	−0.9
CSIRO-Mk3	−2.2	−0.3	−1.9
FGOALS-g	−1.3	1.2	−2.5
GFDL CM3	1.7	**4.7**	−3.0
GISS-E2-H	2.9	1.6	1.3
GISS-E2-R	−0.8	0.3	−1.1
HadGEM2-ES	**−3.5**	**−3.8**	0.4
INM-CM4	−2.6	0.1	−2.7
IPSL-CM5A-MR	−1.4	−2.1	0.6
MIROC5	−2.4	0.6	−3.0
MPI-ESM-LR	−0.8	0.3	−1.1
MRI-CGCM3	**5.0**	3.0	**2.0**
NorESML-M	−2.7	0.7	−3.4
Mean	−0.3	0.9	−1.2

accounts for the majority of total interannual variance in $\overline{P-E}$, while the fraction of variance accounted for by $\overline{E}$ is smaller than for $\overline{P}$ for each subregion and season (Fig. 4).

The ensemble-average downward trend in annually averaged $\overline{P-E}$ across the entirety of SWNA (denoted SWNA/Annual) is $-1.1\,\text{mm month}^{-1}\,\text{century}^{-1}$. It is primarily associated with the downward trend in $\overline{P}$ ($-2.3\,\text{mm month}^{-1}\,\text{century}^{-1}$), consistent with a conclusion of Seager et al. (2007) based on CMIP3 simulations (Table 2). However, by considering the individual effects of $\overline{P}$ and $\overline{E}$ regionally and seasonally, we find that the principal cause of the trend toward aridity in $\overline{P-E}$ is not uniform across SWNA throughout the year.

SWNA aridification is more pronounced in the cold season, relative to smaller $\overline{P-E}$ trends in the warm season, for both North/Cold and South/Cold (Table 2). The biggest downward trend in $\overline{P-E}$ occurs in South/Cold and is caused by a decrease in $\overline{P}$, while $\overline{E}$ also decreases over time providing some compensation in $\overline{P-E}$. The drying trend for North/Cold is primarily caused by an increase in $\overline{E}$, while a small but statistically insignificant decrease in $\overline{P}$ also contributes to aridification. Gutzler and Keller (2012) found that such a trend is already evident in assimilated data from recent decades, associated with diminished snowpack that is melting earlier in the year. The less pronounced trend toward aridification in the warm season is caused by downward trends in $\overline{P}$ in both North and South, while $\overline{E}$ decreases over time (Table 2).

Next we compare the projected $\overline{P-E}$ time series to interannual variability with the RCP8.5 trend removed. The linear trend in $\overline{P-E}$ is calculated over the projected (2006–2100) portion of the normalized time series for North/Cold, South/Cold, North/Warm, and South/Warm (Fig. 5). Twenty-first century aridification is most pronounced in the cold season, when projected $\overline{P-E}$ for both North/Cold and South/Cold consistently drops below the simulated historical average ($y = 0$) (Figs. 5a,c). The trend (red dashed line) is subtracted from the 2006–2100 normalized $\overline{P-E}$ time series (hereafter projected $\overline{P-E}$; red line) in order to calculate a detrended 2006–2100 time series (hereafter detrended $\overline{P-E}$; blue line) and range of interannual variability (light blue shading) for each subregion and season.

The range of interannual variability in cold season $\overline{P-E}$ is largest in North/Cold, during the primary precipitation season there (Figs. 5a,c). Cold season downward trends in $\overline{P-E}$ are large compared to the range of interannual variability and account for a considerable fraction (21% in South/Cold and 14% in North/Cold) of the total interannual variance in cold season $\overline{P-E}$.

The biggest difference between the projected and detrended $\overline{P-E}$ time series occurs in South/Cold, where the downward trend in $\overline{P-E}$ is large and the range of interannual variability is relatively small. South/Cold $\overline{P-E}$ begins to drop below the range of interannual variability around midcentury and lies completely outside of it by 2100 (Fig. 5c). The projected cold season $\overline{P-E}$ for North/Cold stays within the relatively large range of interannual variability until about 2090 (Fig. 5a). However, wet anomalies (when projected $\overline{P-E} > 0$) become less frequent throughout the twenty-first century, indicating that the downward trend in North/Cold $\overline{P-E}$ starts to inhibit drought recovery before 2090.

Changes in aridity are smaller in the warm season surface moisture balances of both North and South; trends account for 1% or less of the total interannual variance in either subregion. With the exception of a few anomalously dry years, warm season $\overline{P-E}$ for both North/Warm and South/Warm stays within the range of interannual variability throughout the twenty-first century (Figs. 5b,d). The ranges of interannual variability in warm season $\overline{P-E}$ are similar to the cold season ranges for North/Cold and South/Cold, except the range is bigger for South/Warm (the primary precipitation season there) than for North/Warm (Figs. 5b,d).

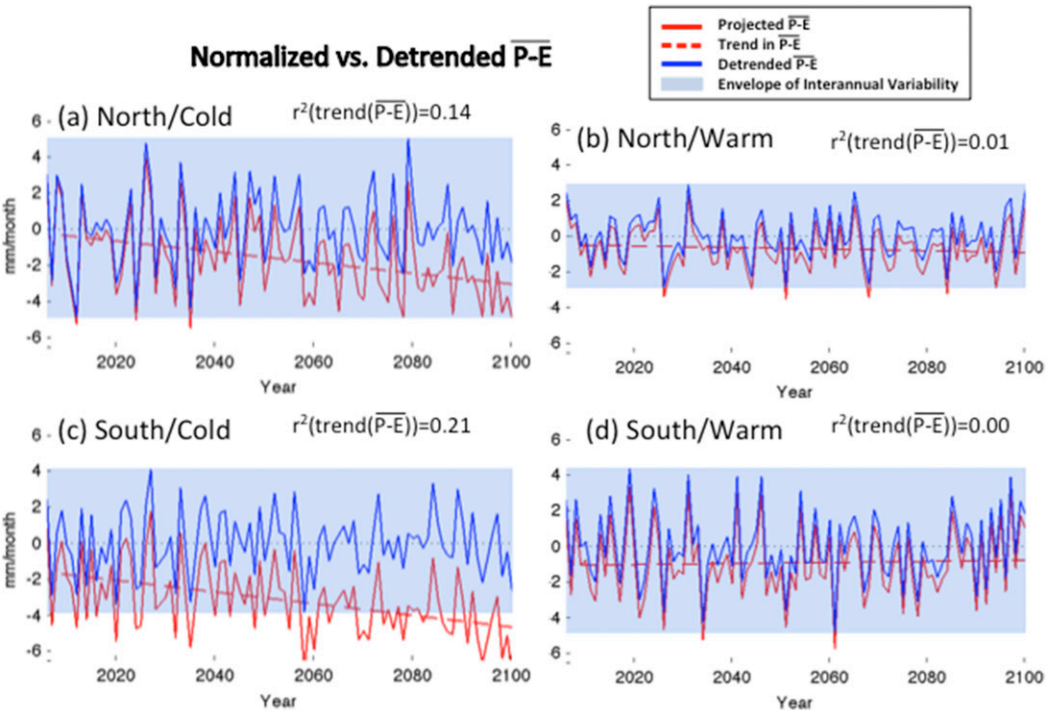

FIG. 5. Ensemble mean projected $\overline{P-E}$ (red line, mm month^{-1}) is shown for the SWNA North and SWNA South subregions during the cold (December–May) and warm (June–November) half-yearly seasons. Projected $\overline{P-E}$ is shown relative to the 1861–1960 simulated historical mean ($y = 0$). Detrended time series (blue line) are calculated by removing the 2006–2100 linear trend (red dashed line) from the projected $\overline{P-E}$ time series. The range of interannual variability (light blue shading) includes all values between the minimum and maximum values of the detrended time series. The fraction of the variance in the projected $\overline{P-E}$ that is accounted for by the projected trend in $\overline{P-E}$ is shown for each subregion and season.

4. Interannual variability of the surface moisture balance

The percentage of the 18 CMIP5 simulations that yield significant correlations between SWNA *P* and *T* in NA, NP, and TP is shown for the historical and RCP8.5 periods for each subregion and season (Table 4). Most CMIP5 models show a strong (≥56%) tendency to simulate the ENSO-associated correlation between TP *T* and SWNA *P* in the cold season (Table 4). The number of models that simulate *r*(TPac *T*, SWNA *P*) is higher in the cold season than in the warm season, which is consistent with the observation that ENSO primarily affects *P* in the southwestern United States during the cold season (Gutzler et al. 2002; Llewellyn et al. 2013). This is especially true for North/Cold where the percentage of models that simulate the cold season ENSO correlation is 83% for the historical period and 89% for the RCP8.5 period. The ENSO correlation tends to weaken in the future RCP8.5 period in South/Cold.

The models show a weaker, but still significant, tendency to simulate the cold season correlation between NP *T* and SWNA *P* in North/Cold (67% in historical and 78% in RCP8.5 simulations; Table 4) and in South/Cold (50% in historical and 44% in RCP8.5 simulations; Table 4). The CMIP5 simulations are thus broadly consistent with observation-based results that ENSO plays a primary role in modulating interannual variability of cold season *P* in the southwestern United States (SWNA North subregion), while NP temperature plays a secondary role in terms of simple correlation with SWNA climate variability (Seager et al. 2005). The tendency for the models to simulate a significant NP correlation during the warm season is very weak (≤6%) in both subregions.

The tendency for models to simulate significant correlations between SWNA *P* and *T* in the NA, NP, and TP tends to weaken in the warm season as compared to the cold season. Warm season NA temperature plays a primary role in modulating warm season interannual variability in SWNA *P*, where 39% or less of the CMIP5 models simulate a significant correlation between warm season NA *T* and SWNA *P* (Table 4). CMIP5 models show a weaker tendency to simulate significant

TABLE 4. Percentage of the 18 CMIP5 simulations that yield significant correlations ($\alpha = 0.05$) between SWNA precipitation in the northern or southern subregions and ocean surface air temperature anomalies over the North Atlantic, North Pacific, and tropical Pacific. Correlations are calculated over the historical (Hist; 1861–2005) and RCP8.5 (RCP; 2006–2100) periods. Significant correlations are counted only if $r > 0$ for r(SWNA P, tropical Pacific T) or if $r < 0$ for r(SWNA P, North Pacific T) and r(SWNA P, North Atlantic T).

		Cold season		Warm season	
		North SWNA	South SWNA	North SWNA	South SWNA
North Atlantic	Hist	0%	0%	39%	39%
	RCP	0%	6%	33%	22%
North Pacific	Hist	67%	50%	6%	3%
	RCP	78%	44%	6%	0%
Tropical Pacific	Hist	83%	72%	22%	6%
	RCP	89%	56%	17%	17%

correlations between SWNA P and T in the TP and NP, where these correlations are simulated by 22% or less and 6% or less, respectively, of the models (Table 4).

A majority of models (72%) simulate the observed negative correlation between TP T and NP T during the cold season in the historical and RCP8.5 simulations. The corresponding correlation is much weaker during the warm season, when only 17% of models generate a significant correlation.

In section 3 we showed that most of the total variance in SWNA $\overline{P-E}$ is accounted for by $\overline{P}$ in CMIP5 simulations of climate from 1861–2100. Here, we show that much of the interannual variability in SWNA $\overline{P}$ is related to Pacific Ocean surface air temperature anomalies associated with the equatorial (ENSO) and North Pacific (PDO) in the cold season. Correlations between ocean temperature and continental climate variables are strongest for North/Cold $\overline{P}$, consistent with observations. We find that cold season T anomalies associated with ENSO (TP) and the PDO index (NP) are significantly correlated, which is also consistent with observations. CMIP5 models therefore show skill in realistically simulating the interannual temporal and spatial characteristics associated with equatorial and extratropical Pacific Ocean climate variability indices that modulate SWNA $\overline{P-E}$ variability. This result justifies our comparison between long-term trends and interannual variability in SWNA $\overline{P-E}$ for distinguishing SWNA aridification, related to both P and E, from the episodic ocean-forced P deficits across SWNA that characterize historical droughts.

5. Discussion

An ensemble of 18 CMIP5 climate models projects a transition to a sustained drier climate, defined in terms of $P - E$, across SWNA over the next century. Separating the cause and magnitude of aridification relative to interannual variability between the northern and southern subregions of SWNA, and between the warm and cold half-year seasons, provides guidance for distinguishing long-term aridification from episodic drought. SWNA aridification is most pronounced in the cold season surface moisture balance but has different characteristics in the North and South subregions of SWNA. By parsing the trends and variability in P, E, and $P - E$ from the northern and southern subregions of the largely defined SWNA and by half-year season, we have shown that analysis of SWNA aridification at finer spatial and temporal resolution reveals important differences in the cause and magnitude of drying that are meaningful for future climate change impact analyses of SWNA regional hydroclimate.

Cold season aridification in SWNA North (U.S. portion), where much of the southwestern U.S. river base flows originate as snowpack, is caused by a temperature-driven increase in $\overline{E}$ while the downward trend in $\overline{P}$ is statistically indistinguishable from zero. The transition from cold season snow to rain in SWNA North further promotes $\overline{E}$ as global temperatures increase (Mote 2003; Knowles et al. 2006). A sustained trend toward aridification occurs in North/Cold throughout the twenty-first century, with $\overline{P-E}$ eventually falling below the range of historical interannual variability. Comparing the r^2 values in Fig. 4 and the linear trend coefficients in Table 2, we conclude that the role of $\overline{E}$ in modulating $\overline{P-E}$ variability is small for interannual fluctuations, but accounts for a large fraction of century-scale drying in North/Cold. By diagnosing the downward trend in North/Cold $\overline{P-E}$ as a function of a long-term trend in E, we have shown that twenty-first-century aridification of North/Cold differs significantly from the more episodic, ocean-forced precipitation deficit droughts of the past.

The biggest increase in aridity occurs in South/Cold (mostly northern Mexico) during the cold season and is caused by a downward trend in $\overline{P}$ (Fig. 4, Table 2). This result reproduces a similar result reported in IPCC AR5 (2013), which shows a big decrease in P across Northern

Mexico. Increased aridity in South/Cold, caused by a downward trend in $\overline{P}$, is partially compensated by a downward trend in $\overline{E}$ as the amount of surface moisture available for evaporation decreases. Ocean-forced interannual fluctuations in SWNA $\overline{P}$ are superimposed onto a downward trend in the cold season $\overline{P-E}$ aridification. The role of $\overline{P}$ in modulating $\overline{P-E}$ interannual variability is large over the period 1861–2100; however, the role of the trend in $\overline{P-E}$ becomes increasingly important during the twenty-first century, contributing 21% of the total interannual variance in South/Cold $\overline{P-E}$ over the century. The downward trend in cold season $\overline{P}$, which occurs in the South but not in the North, signals a northward shift of the winter storm track and supports this prediction from Held and Soden (2006).

Warm season aridification in SWNA North and SWNA South is caused by a decrease in $\overline{P}$, partially compensated by the trend in $\overline{E}$, which also decreases as the surface dries out. However, the decrease in warm season $\overline{E}$ is expected to amplify warm season surface warming across SWNA (Cayan et al. 2010; IPCC 2013; Melillo et al. 2014). Warm season aridification, coupled with elevated temperatures, will impact agricultural and ecological water demands as well as the occurrence of heat waves and wildfires throughout the region (Westerling et al. 2006; Williams et al. 2010; Gutzler 2013; Melillo et al. 2014).

In both North and South, downward trends in $\overline{P-E}$ are smaller in the warm season and remain within the envelope of interannual variability throughout the historical and RCP8.5 periods. The trend accounts for 1% or less of the total interannual variance in twenty-first-century warm season $\overline{P-E}$ (Fig. 5), suggesting that $\overline{P}$ will continue to play a primary role in modulating interannual to multidecadal fluctuations of warm season $\overline{P-E}$ over the next century.

Considering P and E separately has implications for assessing the uncertainties in future projected trend toward aridity, considering the differences in the robustness of projected trends in these variables in different seasons (Knutti and Sedláček 2013). Temperature signals are more robust in CMIP5 simulations of future change than precipitation signals, and model-to-model inconsistencies are particularly large for warm season precipitation changes across SWNA. To the extent that aridification is associated with temperature changes, or cold season precipitation shifts, then confidence in the $P-E$ projections should be bolstered. This result also emphasizes the importance for hydroclimatic projections in semiarid regions of improving estimates of E based on projected values of T and P, and other relevant variables such as wind and humidity (Burke et al. 2006; Sheffield et al. 2012).

The CMIP5 models reproduce the observed interannual correlations between SWNA $\overline{P}$ and ocean surface air temperature anomalies associated with ENSO and PDO. This relationship is strongest in North/Cold where variations in the winter storm track heavily modulate seasonal precipitation, but weakens in South/Cold where the cold season P contribution is smaller. The models also show skill in simulating the observed negative correlation between tropical and North Pacific cold season temperature fluctuations associated with ENSO and PDO (Gershunov and Barnett 1998; Mantua and Hare 2002). Simulated correlations associated with SWNA P and the ENSO and PDO indices weaken in the warm season, consistent with observations.

For both averaging regions and seasons, $\overline{P}$ accounts for a larger fraction than $\overline{E}$ of the total variance in 1861–2100 $\overline{P-E}$. Comparing the results in Fig. 4 and Table 4, we conclude that ocean-forced teleconnections, the basic statistics of which seem to be simulated by most CMIP5 models, are correlated with much of the total interannual variance in cold season $\overline{P-E}$ time series for SWNA North and South, especially during the historical (1861–2005) period. The tendency for the models to simulate the ENSO-associated cold season correlation between equatorial Pacific ocean T and SWNA P weakens in the twenty-first century (RCP8.5) simulations, especially in South/Cold. The weaker statistical coupling is consistent with the increasing importance of the $\overline{P}$-driven downward trend in $\overline{P-E}$, whose relative contribution to the total interannual variance in $\overline{P-E}$ increases throughout the twenty-first century as the winter storm track moves north in a warmer climate.

It is important to acknowledge the multiple uncertainties inherent in the use of general circulation models (GCMs) to study the climate system. Many studies have compared GCM output with observations and conclude that the models are skillful at simulating climate patterns that are generated via large-scale dynamics (IPCC 2013). The projected increase in global temperatures, robust among the CMIP5 models, is one example of this (IPCC 2013). Long-term changes in winter precipitation for which we see evidence in the CMIP5 simulations (as documented previously) are another example. This may partly explain why the simulated trends in warm season $\overline{P-E}$ remain small compared to twenty-first century interannual variability, as compared to the cold season.

As our results confirm, output can vary widely among the models, depending on the model resolution, interaction between model components, parameterizations, and other factors. Precipitation simulations tend to differ significantly from one model to the next (Zhang et al. 2007; IPCC 2013). Across SWNA, both winter

storm tracks and summer monsoon development exhibit considerable model-to-model uncertainties in CMIP5 simulations (Chang et al. 2012; Sheffield et al. 2013). As in many previous studies, we consider the average of many simulations to provide the better estimate of expected changes than any individual simulation, and we have not attempted to choose superior simulations. By taking simple arithmetic means of all simulations, we implicitly assume (by default) that the models show equal skill in simulating SWNA P, E, and $P - E$. Much of the individual model variance is averaged out of the ensemble mean; however, we retain the intermodel variations by showing the smoothed interquartile range of $(P - E)'$ in Fig. 4

By considering only the RCP8.5 emissions scenario we maintain a higher level of consistency among the simulations, but we do not include additional uncertainty related to future socioeconomic conditions, technology, public policy, and other factors captured by the full range of different scenarios. Future anthropogenic radiative forcing may deviate significantly from the RCP8.5 trajectory, depending on a variety of social and environmental factors. The RCP8.5 emissions scenario increases radiative forcing faster than most other scenarios, so the RCP8.5 simulations generally exhibit relatively large projected changes in P, E, and $P - E$.

6. Summary and conclusions

We examine SWNA aridification over the period 1861–2100 by comparing warm and cold season trends and interannual variability in P, E, and $P - E$ between the northern, southern, and combined subregions of SWNA using 18 model simulations from the CMIP5 archive. Using this approach, we show that the cause and magnitude of SWNA aridification varies between the warm and cold seasons across the broadly defined region of SWNA. We compare the projected (2006–2100) $\overline{P-E}$ time series to a future without the RCP8.5-associated trends to see how century-scale trends affect twenty-first-century $\overline{P-E}$ relative to the interannual variations that are a normal feature of SWNA climate. We calculate the correlations between seasonal SWNA P and remote ocean temperature anomalies associated with ENSO, PDO, and AMO to infer the mechanisms that generate interannual variability within the CMIP5 models.

SWNA aridification is a robust feature in CMIP5 projections of twenty-first-century $\overline{P-E}$ for the warm and cold half-yearly seasons. This result is consistent with previous analyses of CMIP3 projections (Seager et al. 2007; Hoerling and Eischeid 2007; Gutzler and Robbins 2011) and the hypothesis that dry areas become drier in a warmer climate regime (Held and Soden 2006; IPCC 2013). Our results, based on CMIP5 projections, are consistent with Seager et al.'s (2007) CMIP3-based conclusion that the annually averaged drying trend in $\overline{P-E}$ across the largely defined SWNA (SWNA North + SWNA South) is caused by a downward trend in $\overline{P}$. These prior results have been extended here by parsing the effects of $\overline{P}$ and $\overline{E}$ by subregion and season, showing significant spatial and seasonal variations in SWNA aridification that are important to consider when analyzing the impacts of climate change on SWNA hydrology.

SWNA aridification is distinguished from the droughts of the past because it is caused by long-term trends in P and E that are related to anthropogenic global warming rather than the episodic ocean-forced precipitation deficits that characterize historical SWNA drought. Aridification is most pronounced in the cold season surface moisture balance of each subregion, which drops below the range of interannual variability by the end of the twenty-first century. The downward trend in cold season $\overline{P-E}$ is caused by increasing $\overline{E}$ in North/Cold and by decreasing $\overline{P}$ in South/Cold. ENSO and PDO ocean-based indices modulate interannual fluctuations in cold season SWNA P that are superimposed over the century-scale drying trends in CMIP5 projections of twenty-first-century climate.

Downward trends in $P - E$ are much smaller in the warm season, in terms of both absolute magnitude of the projected trends and as a fraction of total interannual variability. These trends are associated with decreases in precipitation in both North/Warm and South/Warm. Warm season $\overline{P-E}$ remains within the range of interannual variability throughout the twenty-first century in both subregions, but still contributes to changes in local temperatures, wildfire frequency, and ecological water demands. Together, the warm and cold season projections of SWNA $\overline{P-E}$ foretell a future of sustained drier conditions that will exacerbate water scarcity issues across SWNA over the next century.

Acknowledgments. Preliminary results were supported by a grant from the National Science Foundation. We acknowledge the World Climate Research Programme's Working Group on Coupled Modelling, which is responsible for CMIP5. We thank the climate modeling groups listed in Table 1 for producing and making available their model output. The U.S. Department of Energy's Program for Climate Model Diagnosis and Intercomparison provides coordinating support for CMIP5 and led development of software infrastructure in partnership with the Global Organization for Earth System Science Portals. We thank

R. Seager for helpful comments and two anonymous reviewers who provided exceptionally thorough and helpful criticism.

REFERENCES

Barnett, T. P., and Coauthors, 2008: Human-induced changes in the hydrology of the western United States. *Science*, **319**, 1080–1083, doi:10.1126/science.1152538.

Bellenger, H., E. Guilyardi, J. Leloup, M. Lengaigne, and J. Vialard, 2014: ENSO representation in climate models: From CMIP3 to CMIP5. *Climate Dyn.*, **42**, 1999–2018, doi:10.1007/s00382-013-1783-z.

Burke, E. J., S. J. Brown, and N. Christidis, 2006: Modeling the recent evolution of global drought and projections for the twenty-first century with the Hadley Centre climate model. *J. Hydrometeor.*, **7**, 1113–1125, doi:10.1175/JHM544.1.

Cayan, D. R., T. Das, D. W. Pierce, T. P. Barnett, M. Tyree, and A. Gershunov, 2010: Future dryness in the southwest US and the hydrology of the early 21st century drought. *Proc. Natl. Acad. Sci. USA*, **107**, 21 271–21 276, doi:10.1073/pnas.0912391107.

Chang, E. K., Y. Guo, and X. Xia, 2012: CMIP5 multimodel ensemble projection of storm track change under global warming. *J. Geophys. Res.*, **117**, D23118, doi:10.1029/2012JD018578.

Cook, B. I., and R. Seager, 2013: The response of the North American monsoon to increased greenhouse gas forcing. *J. Geophys. Res. Atmos.*, **118**, 1690–1699, doi:10.1002/jgrd.50111.

——, T. R. Ault, and J. E. Smerdon, 2015: Unprecedented 21st-century drought risk in the American Southwest and Central Plains. *Sci. Adv.*, **1**, e1400082, doi:10.1126/sciadv.1400082.

Douglas, M. W., R. A. Maddox, K. Howard, and S. Reyes, 1993: The Mexican monsoon. *J. Climate*, **6**, 1665–1677, doi:10.1175/1520-0442(1993)006<1665:TMM>2.0.CO;2.

Garfin, G., G. Franco, H. Blanco, A. Comrie, P. Gonzalez, T. Piechota, R. Smyth, and R. Waskom, 2014: Southwest. *Climate Change Impacts in the United States: The Third National Climate Assessment*, J. M. Melillo, T. C. Richmond, and G. W. Yohe, Eds., U.S. Global Change Research Program, 462–486, doi:10.7930/J08G8HMN.

Gershunov, A., and T. P. Barnett, 1998: Interdecadal modulation of ENSO teleconnections. *Bull. Amer. Meteor. Soc.*, **79**, 2715–2725, doi:10.1175/1520-0477(1998)079<2715:IMOET>2.0.CO;2.

Gutzler, D. S., 2013: Regional climatic considerations for borderlands sustainability. *Ecosphere*, **4**, 7, doi:10.1890/ES12-00283.1.

——, and T. O. Robbins, 2011: Climate variability and projected change in the western United States: Regional downscaling and drought statistics. *Climate Dyn.*, **37**, 835–849, doi:10.1007/s00382-010-0838-7.

——, and S. J. Keller, 2012: Observed trends in snowpack and spring season soil moisture affecting New Mexico. *New Mexico J. Sci.*, **46**, 169–172.

——, D. M. Kann, and C. Thornbrugh, 2002: Modulation of ENSO-based long-lead outlooks of southwestern U.S. winter precipitation by the Pacific decadal oscillation. *Wea. Forecasting*, **17**, 1163–1172, doi:10.1175/1520-0434(2002)017<1163:MOEBLL>2.0.CO;2.

——, and Coauthors, 2009: Simulations of the North American monsoon: NAMAP2. *J. Climate*, **22**, 6716–6740, doi:10.1175/2009JCLI3138.1.

Held, I. M., and B. J. Soden, 2006: Robust responses of the hydrological cycle to global warming. *J. Climate*, **19**, 5686–5699, doi:10.1175/JCLI3990.1.

Higgins, R. W., Y. Chen, and A. V. Douglas, 1999: Interannual variability of the North American warm season precipitation regime. *J. Climate*, **12**, 653–679, doi:10.1175/1520-0442(1999)012<0653:IVOTNA>2.0.CO;2.

Hoerling, M., and J. Eischeid, 2007: Past peak water in the Southwest. *Southwest Hydrology*, Vol. 6 (1), University of Arizona, Tucson, AZ, 18 ff. [Available online at http://www.swhydro.arizona.edu/archive/V6_N1/.]

IPCC, 2013: *Climate Change 2013: The Physical Science Basis.* T. F. Stocker et al., Eds., Cambridge University Press, 1535 pp.

Kim, H.-M., P. J. Webster, and J. A. Curry, 2012: Evaluation of short-term climate change prediction in multi-model CMIP5 decadal hindcasts. *Geophys. Res. Lett.*, **39**, L10701, doi:10.1029/2012GL051644.

Knowles, N., M. D. Dettinger, and D. R. Cayan, 2006: Trends in snowfall versus rainfall in the western United States. *J. Climate*, **19**, 4545–4559, doi:10.1175/JCLI3850.1.

Knutti, R., and J. Sedláček, 2013: Robustness and uncertainties in the new CMIP5 climate model projections. *Nat. Climate Change*, **3**, 369–373, doi:10.1038/nclimate1716.

Larson, J., Y. Zhou, and R. W. Higgins, 2005: Characteristics of landfalling tropical cyclones in the United States and Mexico: Climatology and interannual variability. *J. Climate*, **18**, 1247–1262, doi:10.1175/JCLI3317.1.

Llewellyn, D. K., S. Vaddey, J. D. Roach, and A. Pinson, 2013: Westwide climate risk assessment: Upper Rio Grande impact assessment. U.S. Department of Interior, Bureau of Reclamation, Upper Colorado Region, Albuquerque Area Office, 169 pp.

Mantua, N. J., and S. R. Hare, 2002: The Pacific decadal oscillation. *J. Oceanogr.*, **58**, 35–44, doi:10.1023/A:1015820616384.

McCabe, G. J., M. A. Palecki, and J. L. Betancourt, 2004: Pacific and Atlantic Ocean influences on multidecadal drought frequency in the United States. *Proc. Natl. Acad. Sci. USA*, **101**, 4136–4141, doi:10.1073/pnas.0306738101.

Meinshausen, M., and Coauthors, 2011: The RCP greenhouse gas concentrations and their extensions from 1765 to 2300. *Climatic Change*, **109**, 213–241, doi:10.1007/s10584-011-0156-z.

Melillo, J. M., T. C. Richmond, and G. W. Yohe, 2014: *Climate Change Impacts in the United States: The Third National Climate Assessment*. U.S. Global Change Research Program, 841 pp., doi:10.7930/J0Z31WJ2.

Moss, R. H., and Coauthors, 2010: The next generation of scenarios for climate change research and assessment. *Nature*, **463**, 747–756, doi:10.1038/nature08823.

Mote, P. W., 2003: Trends in snow water equivalent in the Pacific Northwest and their climatic causes. *Geophys. Res. Lett.*, **30**, 1601, doi:10.1029/2003GL017258.

NOAA, 2014: 6-month climatology maps. Accessed 5 May 2014. [Available online at http://www.drought.gov/nadm/content/climatology-6-month.]

Ropelewski, C., and M. Halpert, 1986: North American precipitation and temperature patterns associated with the El Niño/Southern Oscillation (ENSO). *Mon. Wea. Rev.*, **114**, 2352–2362, doi:10.1175/1520-0493(1986)114<2352:NAPATP>2.0.CO;2.

Schubert, S., and Coauthors, 2009: A U.S. CLIVAR project to assess and compare the responses of global climate models to drought-related SST forcing patterns: Overview and results. *J. Climate*, **22**, 5251–5272, doi:10.1175/2009JCLI3060.1.

Seager, R., and G. A. Vecchi, 2010: Greenhouse warming and the 21st century hydroclimate of southwestern North America.

Proc. Natl. Acad. Sci. USA, **107**, 21 277–21 282, doi:10.1073/pnas.0910856107.

——, Y. Kushnir, C. Herweijer, N. Naik, and J. Velez, 2005: Modeling of tropical forcing of persistent droughts and pluvials over western North America: 1856–2000. *J. Climate*, **18**, 4065–4088, doi:10.1175/JCLI3522.1.

——, and Coauthors, 2007: Model projections of an imminent transition to a more arid climate in southwestern North America. *Science*, **316**, 1181–1184, doi:10.1126/science.1139601.

——, and Coauthors, 2014: Dynamical and thermodynamical causes of large-scale changes in the hydrological cycle over North America in response to global warming. *J. Climate*, **27**, 7921–7948, doi:10.1175/JCLI-D-14-00153.1.

——, M. Hoerling, S. Schubert, H. Wang, B. Lyon, A. Kumar, J. Nakamura, and N. Henderson, 2015: Causes of the 2011–14 California drought. *J. Climate*, **28**, 6997–7024, doi:10.1175/JCLI-D-14-00860.1.

Seidel, D. J., Q. Fu, W. J. Randel, and T. J. Reichler, 2008: Widening of the tropical belt in a changing climate. *Nat. Geosci.*, **1**, 21–24, doi:10.1038/ngeo.2007.38.

Seneviratne, S. I., and Coauthors, 2012: Changes in climate extremes and their impacts on the natural physical environment. *Managing the Risks of Extreme Events and Disasters to Advance Climate Change Adaptation*, C. B. Field et al., Eds., Cambridge University Press, 109–230.

Serreze, M. C., M. P. Clark, R. L. Armstrong, D. A. McGinnis, and R. S. Pulwarty, 1999: Characteristics of the western United States snowpack from snowpack telemetry (SNOTEL) data. *Water Resour. Res.*, **35**, 2145–2160, doi:10.1029/1999WR900090.

Sheffield, J., E. F. Wood, and M. L. Roderick, 2012: Little change in global drought over the past 60 years. *Nature*, **491**, 435–438, doi:10.1038/nature11575.

——, and Coauthors, 2013: North American climate in CMIP5 experiments. Part I: Evaluation of historical simulations of continental and regional climatology. *J. Climate*, **26**, 9209–9245, doi:10.1175/JCLI-D-12-00592.1.

Stevenson, S. L., 2012: Significant changes to ENSO strength and impacts in the twenty-first century: Results from CMIP5. *Geophys. Res. Lett.*, **39**, L17703, doi:10.1029/2012GL052759.

Swetnam, T. W., and J. L. Betancourt, 1998: Mesoscale disturbance and ecological response to decadal climatic variability in the American Southwest. *J. Climate*, **11**, 3128–3147, doi:10.1175/1520-0442(1998)011<3128:MDAERT>2.0.CO;2.

Taylor, K. E., R. J. Stouffer, and G. A. Meehl, 2012: An overview of CMIP5 and the experiment design. *Bull. Amer. Meteor. Soc.*, **93**, 485–498, doi:10.1175/BAMS-D-11-00094.1.

Wang, S.-Y., L. Hipps, R. R. Gillies, and J.-H. Yoon, 2014: Probable causes of the abnormal ridge accompanying the 2013–2014 California drought: ENSO precursor and anthropogenic warming footprint. *Geophys. Res. Lett.*, **41**, 3220–3226, doi:10.1002/2014GL059748.

Weiss, J. L., C. L. Castro, and J. T. Overpeck, 2009: Distinguishing pronounced droughts in the southwestern United States: Seasonality and effects of warmer temperatures. *J. Climate*, **22**, 5918–5932, doi:10.1175/2009JCLI2905.1.

Westerling, A. L., H. G. Hidalgo, D. R. Cayan, and T. W. Swetnam, 2006: Warming and earlier spring increase western US forest wildfire activity. *Science*, **313**, 940–943, doi:10.1126/science.1128834.

Williams, A. P., C. D. Allen, C. I. Millar, T. W. Swetnam, J. Michaelsen, C. J. Still, and S. W. Leavitt, 2010: Forest responses to increasing aridity and warmth in the southwestern United States. *Proc. Natl. Acad. Sci. USA*, **107**, 21 289–21 294, doi:10.1073/pnas.0914211107.

Woodhouse, C. A., D. M. Meko, G. M. MacDonald, D. W. Stahle, and E. R. Cook, 2010: Climate change and water in southwestern North America special feature: A 1,200-year perspective of 21st century drought in southwestern North America. *Proc. Natl. Acad. Sci. USA*, **107**, 21 283–21 288, doi:10.1073/pnas.0911197107.

Yin, J. H., 2005: A consistent poleward shift of the storm tracks in simulations of 21st century climate. *Geophys. Res. Lett.*, **32**, L18701, doi:10.1029/2005GL023684.

Zhang, X., F. W. Zwiers, G. C. Hegerl, F. H. Lambert, N. P. Gillett, S. Solomon, P. A. Stott, and T. Nozawa, 2007: Detection of human influence on twentieth-century precipitation trends. *Nature*, **448**, 461–465, doi:10.1038/nature06025.